

The impact of correlated projections on weak lensing cluster counts

Laura Marian¹, Robert E. Smith², Gary M. Bernstein³

¹*Argelander-Institut für Astronomie, Universität Bonn, Bonn, D-53121, Germany*

²*Institute for Theoretical Physics, University of Zürich, Zürich, CH 8037, Switzerland*

³*Department of Physics and Astronomy, University of Pennsylvania, Philadelphia, PA 19104, USA*

Large-scale structure projections are an obstacle in converting the shear signal of clusters detected in weak-lensing maps into virial masses. However, this step is not necessary for constraining cosmology with the shear-peak abundance, if we are able to predict its amplitude. We generate a large ensemble of N -body simulations spanning four cosmological models, with total volume $V_{\text{tot}} \sim 1[h^{-1} \text{Gpc}]^3$ per model. Variations to the matter density parameter and amplitude of fluctuations are considered. We measure the abundance of peaks in the mass density projected in $\approx 100 h^{-1} \text{Mpc}$ slabs to determine the impact of structures spatially correlated with the simulation clusters, identified by the 3D friends-of-friends algorithm. The halo model shows that the choice of the smoothing filter for the density field is important in reducing the contribution of correlated projections to individual halo masses. Such contributions are less than 2% in the case of the optimal, compensated filter used throughout this analysis. We measure the change in the mass of peaks when projected in slabs of various thicknesses. Peaks in slabs of $26 h^{-1} \text{Mpc}$ and $102 h^{-1} \text{Mpc}$ suffer an average mass change of less than 2% compared to their mass in slabs of $51 h^{-1} \text{Mpc}$. We then explore the cosmology dependence of the projected-peak mass function, and find that, for a wide range of slab thicknesses ($< 500 h^{-1} \text{Mpc}$), it scales with cosmology in exactly the same way as the 3D friends-of-friends mass function and the Sheth-Tormen formula. This extends the earlier result of Marian *et al.* [22]. Finally, we show that for all cosmological models considered, the low and intermediate mass bins of the peak abundance can be described using a modified Sheth-Tormen functional form to within 10%-20% accuracy.

I. INTRODUCTION

For more than a decade, weak gravitational lensing (WL) has been considered a powerful probe for testing the cosmological framework. The basic idea of gravitational lensing is that on its way to the observer, the light from distant sources is deflected by the intervening matter along the line of sight. On average these deflections are very small, so the result in most cases is that a circular source galaxy looks slightly elliptical, i.e. the image of the source is sheared. Images can also be magnified. For a quantitative idea, the shear is typically of about 2%, hence the name of WL. By measuring the shear, we can map the 3D matter distribution of the universe in an unbiased way, independent of baryonic matter tracers. Indeed, the largest surveys to date aimed at measuring cosmic shear, from CTIO (Jarvis *et al.* [16, 17]) and more recently the CFHTLS (Hoekstra *et al.* [14], Semboloni *et al.* [35]), have demonstrated the potential of WL to place important constraints on the cosmological model. In particular, the CTIO results were among the first to indicate that the normalization of mass fluctuations was lower ($\sigma_8 \approx 0.8$) than the WMAP1 (Spergel *et al.* [38]) analysis suggested ($\sigma_8 \approx 0.9$), a finding confirmed now by the WMAP5 analysis (Komatsu *et al.* [18]).

In this study, we concentrate on WL-detected clusters. WL identifies clusters as peaks in shear maps. The cluster abundance is one of the four most promising tools to measure dark energy (Albrecht *et al.* [2]), together with supernova surveys, baryonic acoustic oscillations, and WL surveys. The cluster abundance is sensitive to the redshift dependence of the angular diameter dis-

tance, the time dependence of the expansion rate and the growth rate of structure. There are three very appealing features of WL-detected clusters:

1. The shear is straightforward to predict, given a model of structure formation. This is not the case for X-ray, Sunyaev-Zeldovich, or optical clusters, for which the conversion from measurable quantities—flux, temperature, decrement—to virial masses depends on the complex gas physics of baryons in clusters. Cosmological constraints are likely to be biased if the mass-observable relation evolves with redshift in a way that mimics cosmological changes.
2. An immediate consequence of the first point is that shear peaks are easily studied from numerical simulations of dark matter, since they are not very sensitive to the baryonic matter distribution. This is a huge advantage over the other cluster methods, because dark matter simulations are relatively cheap to produce with the current computer technology, whereas simulating the evolution of baryons depends on poorly known astrophysics and is computationally very demanding and expensive.
3. Finally, shear peaks come “for free”, i.e. a survey designed to measure the “cosmic shear” 2-point function can detect clusters without much additional observational effort.

One issue that has raised concerns about the utility of WL clusters is the projection effect: the 2D shear maps

encode the 3D matter distribution information. If a cluster produces a detectable signal in a lensing map, then to this signal contributes not only the mass of the cluster, but also the matter along the line of sight. This matter, external to the cluster itself, can be either nearby it, and therefore spatially correlated with it, or it can be at such a large separation that there is no correlation with the cluster. Hence, we can divide contributions from external matter along the line of sight into *correlated* and *uncorrelated projections*. Thus, reconstructing the mass of a cluster can be challenging as there is no predefined way to separate its shear signal from that induced by other structures on the same line of sight.

Many theoretical and numerical endeavors have been aimed at estimating the magnitude of this effect, its impact on cluster mass reconstructions, and on the cosmological constraints derived from the WL-detected cluster abundance. Here we just mention a few of these works. Hoekstra [13] used the aperture mass statistic, introduced by Schneider [31], to evaluate the uncertainty in cluster mass estimates due to the uncorrelated large-scale structure (LSS) contamination. For large clusters at $z = 0.1$, they found the uncertainty to be $\approx 6\%$.

Other numerical studies have focused on the efficiency of WL surveys to detect clusters. Hamana *et al.* [11] compared the signal-to-noise (S/N) of the peaks measured from simulated convergence maps to the Navarro-Frenk-White (NFW) (Navarro *et al.* [27]) S/N of the 3D clusters producing the peaks. They found scatter and bias in the predicted vs. measured S/N relation, which they explained through both departures of the 3D halo density profiles from the spherically symmetric NFW, as well as LSS projections. Tang and Fan [40] also attributed a similar scatter to the asphericity of halos, and to halo substructure. De Putter and White [8] concluded that individual cluster shear measurements are contaminated by projections of very small clusters along the line of sight, i.e. halos with masses smaller than $10^{12} h^{-1} M_{\odot}$. Hennawi and Spergel [12] performed an extensive numerical study of the WL-cluster detection. The authors used tomographic information to determine the redshifts of the lenses, along with an optimal filter to enhance the cluster detection. One of their results was that even in the absence of the intrinsic ellipticity noise – which is known to produce spurious peaks, see for instance Hamana *et al.* [11] – about 15% of the most significant peaks were due to LSS projections, and not to any halo in particular. Dodelson [10] and Maturi *et al.* [23] have independently proposed optimal linear estimators with a shape designed to filter out the LSS contributions. Maturi *et al.* [23] used N -body simulations to compare their estimator, which is formally an aperture mass estimator, to the standard aperture mass filter, proposed by Schneider *et al.* [32] for measurements of cosmic shear. The numerical tests have indicated their filter to be more efficient than the standard aperture mass at discarding ‘false positives’, i.e. those shear peaks arising from LSS projections. Schirmer *et al.* [30] and Maturi *et al.* [24] detected clusters in shear

data and found the performance of the optimal filter of Maturi *et al.* [23] to be similar to that of the aperture mass statistic used with a NFW-matched filter. Another example of cluster detection in shear data is the work of Abate *et al.* [1].

Marian and Bernstein [21] also used an optimal shear filter to forecast WL-cluster constraints for future ground- and space-based surveys. They found that cosmological constraints are not severely altered by uncorrelated LSS projections. One of the critical assumptions that forecasts adopt (see also Wang *et al.* [41]) is to consider the Sheth-Tormen (ST) (Sheth and Tormen [36]) mass function a proxy for the shear-peak mass function. But is the shear-peak mass function as sensitive to cosmology as the 3D one? In a pioneering study by Reblinsky *et al.* [29], reasonable agreement was found between the analytic predictions from the model of Kruse and Schneider [20] and peak counts measured from numerical simulations. However, the small sample volumes studied, $V_{\text{tot}} \sim 10^{-3} [h^{-1} \text{Gpc}]^3$, limited the statistical power of the conclusions, especially for application to future WL data sets. In a recent analysis (Marian *et al.* [22]), we used a very large ensemble of numerical simulations to pursue the issue further. We showed that the 2D mass function of peaks projected in thin slabs scales with cosmology in the same way as the measured 3D mass function, and also as the ST prediction. Owing to the large total volume $V_{\text{tot}} \sim 1 [h^{-1} \text{Gpc}]^3$ per cosmological model, the result was established at very high statistical significance. This suggests that for the purpose of constraining cosmology, one can avoid the difficult task of converting shear peaks into cluster masses. If the cosmology dependence of the shear peaks is understood, one needs only measure their abundance to obtain the desired constraints. Dietrich and Hartlap [9] took this approach numerically and derived constraints from shear peaks measured from simulations with the aperture mass statistic. See also the related work of Kratochvil *et al.* [19], and Pires *et al.* [28].

In this paper we continue our investigation of the effect of correlated mass structures on the projected-peak mass function and its power to constrain cosmological models.

To achieve this goal, we use numerical simulations. For each simulation box we divide the matter density field across the line of sight up into slabs. Our observable is the density field projected into such slabs. If the slabs are thin, this observable is equivalent to the WL convergence – defined as the surface mass density scaled by the critical surface mass density, Σ_{crit} . Even when the slabs get thicker (256, 512 $h^{-1} \text{Mpc}$), the critical surface mass density varies only a few percents of its central value for typical lenses and sources in the ΛCDM model, as pointed out by Metzler *et al.* [25]. The reason we are interested in slabs is that, by definition, we expect only the matter in a limited spatial volume around a main cluster lens to give rise to correlated projections. We underline that uncorrelated projections are the subject of a future study, and not of this study.

We extend the analysis of Marian *et al.* [22] in a number of important ways. Firstly, we apply the halo model of structure formation to quantify the expected mass increase arising from correlated structures along the line of sight. Secondly, we generalize our earlier results through studying the projected peak mass function in slabs of various thicknesses. Thirdly, we show how the projected-peak mass function can be modeled.

The paper is structured as follows. In section §II we present the numerical simulations that our study is based upon; in §III we use the halo model to predict the change in peak masses due to correlated projections and in §IV we describe the optimal filter that we apply to the data. In §V we show how we find and select the density peaks. Section §VII contains the main results of our study, and in §VIII we draw our conclusions. Finally, we would like to clarify the mass definitions that we use throughout this work. We shall refer to those masses measured using full 3D information, as 3D masses (M_{3D}). Similarly, 2D masses are measured from 2D data (M_{2D}). Depending on the context, M_{3D} is usually either the virial mass defined by ST, or the mass defined by the friends-of-friends (FoF) algorithm of Davis *et al.* [7]. We shall specify the meaning of the notation M_{3D} in the context where we use it. M_{2D} will always mean the mass of a projected peak, and the way we assign masses to projected peaks is described in section §IV.

II. NUMERICAL SIMULATIONS

We have generated an ensemble of 32 N -body simulations for 4 different cosmological models, with 8 realizations per model. The simulations were run using **Gadget-2** (Springel [39]), and they have 400^3 particles of mass $m_p \approx 10^{11} h^{-1} M_\odot$ in a simulated volume of $512^3 (h^{-1} \text{Mpc})^3$. The full details are in Table I. There are 18 snapshots, logarithmically spaced in the scale factor a , between redshifts 50 and 0. We used the **2LPT** code of Scoccimarro [33] to generate the initial conditions for the density fluctuations. For each of the 8 realizations, the initial conditions for the 4 cosmologies are the same. Thus, the cosmic variance on the comparison of measured quantities in different cosmologies will be minimal. The transfer function was taken from **cmbfast** (Seljak and Zaldarriaga [34]) (the output at redshift 0). We identified the simulation halos using the FoF algorithm, with $b = 0.2$, where b is the fraction of the inter-particle separation. The smallest of our halos have 30 particles. Our fiducial cosmology is described by Model 1 in Table I. We shall refer to the other models as the variational cosmologies.

TABLE I: Numerical simulation details. Top-table columns are: matter, dark energy, and baryon density parameters; normalization of fluctuations; mass per particle in units of ($10^{11} h^{-1} M_\odot$); number of realizations. Bottom-table columns show: box length; dark energy equation of state $w = p_{DE}/\rho_{DE}$; number of particles; Hubble's constant in units of $100 \text{ km s}^{-1} \text{ Mpc}^{-1}$; baryon fraction.

	Ω_m	Ω_{DE}	Ω_b	σ_8	m_p	N_{run}
Model 1	0.27	0.73	0.0460	0.9	1.57	8
Model 2	0.22	0.78	0.0375	0.9	1.28	8
Model 3	0.27	0.73	0.0460	0.75	1.57	8
Model 4	0.32	0.68	0.0545	0.9	1.86	8

$L = 512 h^{-1} \text{Mpc}$ $w = -1$ $N_p = 400^3$ $h = 0.72$ $f_b = 17\%$

III. THEORETICAL PREDICTION OF THE CORRELATED PROJECTION EFFECT

In this section we develop a theoretical prediction for the correlated projection effect. We base our calculation for the correlated projections on the halo model, and we rigorously test it against numerical simulations. Our approach is the following: we test the strength of the projection effect in slabs of various thickness. For a cluster at the center of such a slab, we expect that the contribution from structures correlated with it will flatten out as we increase the slab thickness. Only those objects within the correlation length of the cluster ($r_0 \sim 30 h^{-1} \text{Mpc}$ for clusters more massive than $10^{14} h^{-1} M_\odot$) will affect its lensing signal. As the slab thickness becomes large – a few hundreds Mpc – it is reasonable to assume that chance or uncorrelated projections will start to contribute.

If the large-scale distribution of the mass in the Universe were perfectly described by the halo model, then all the mass would be contained in halos with universal properties: spherical symmetry, a universal density profile, and a mass function; see [5] for a halo model review. In this framework, we would like to estimate the average contribution to the projected density of a halo of mass M_1 from structures correlated with it. The probability of finding a halo with mass in the interval $(M_2, M_2 + dM_2)$, within a range $(\mathbf{r}, \mathbf{r} + d^3\mathbf{r})$ of the center of M_1 is given by:

$$\mathcal{P}(\mathbf{r}, M_2 | M_1) dM_2 d^3\mathbf{r} = n(M_2) [1 + \xi_\times(\mathbf{r}, M_2 | M_1)] dM_2 d^3\mathbf{r}, \quad (1)$$

where $n(M_2)$ is the halo mass function, i.e. the comoving number density of halos of mass M_2 per unit mass, and ξ_\times is the cross-correlation between the center of halo M_1 and the mass distribution of M_2 . The expected density profile of matter *external* to the halo M_1 is:

$$\langle \rho_{\text{ext}}(\mathbf{r} | M_1) \rangle = \int dM_2 M_2 n(M_2) [1 + \xi_\times(\mathbf{r}, M_2 | M_1)]. \quad (2)$$

The cross-correlation function can be obtained from the

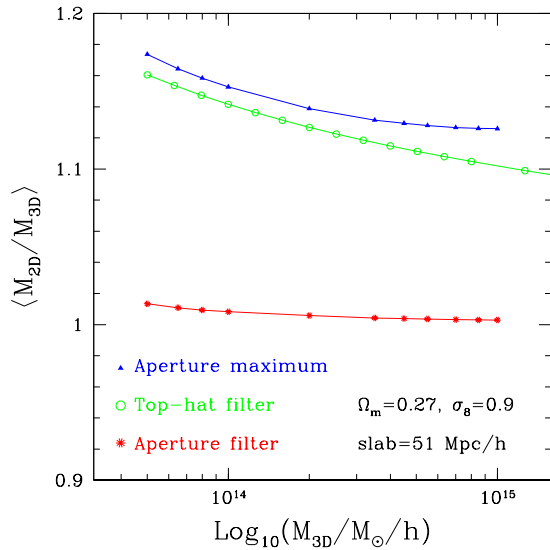


FIG. 1: The change in mass due to correlated projections as a function of the Sheth-Tormen virial mass. The starred red symbols correspond to the optimal compensated filter described in section §IV, and the empty green circles to the top-hat filter. These curves are for a slab thickness of $51 h^{-1}$ Mpc. The blue triangles show the maximum correlated projection effect for the compensated filter, as given by Eq. (10). This plot corresponds to the fiducial cosmology.

cross-power spectrum:

$$\xi_{\times}(\mathbf{r}, M_2|M_1) = \int \frac{dk}{2\pi^2} k^2 P_{\times}(k, M_2|M_1) j_0(kr), \quad (3)$$

where $j_0(x) = \sin(x)/x$ is the zero-order spherical Bessel function. The halo center cross-power spectrum, at leading order in the halo perturbation theory, is:

$$P_{\times}(k, M_2|M_1) = b(M_1) b(M_2) U(k, M_2) P(k), \quad (4)$$

where $b(M)$ is the first order linear bias parameter, $P(k)$ is the nonlinear matter power spectrum. $U(k, M)$ is the Fourier transform of the 3D density profile of a halo with mass M :

$$\begin{aligned} U(k, M) &\equiv \frac{\rho(k, M)}{M}, \\ &= \frac{4\pi}{M} \int_0^{R_{\text{vir}}} dr r^2 \rho(r, M) j_0(kr). \end{aligned} \quad (5)$$

In the above, we have assumed that the 3D density profile of the halo is cut off at the virial radius R_{vir} . The expected projected mass density external to the halo with mass M_1 is the integral of Eq.(2) along the projection axis – for example the \hat{z} direction:

$$\langle \Sigma_{\text{ext}}(\mathbf{r}_{\perp}|M_1) \rangle = 2 \int_{\sqrt{R_{\text{vir}}(M_1)^2 - r_{\perp}^2}}^{L/2} dz \langle \rho_{\text{ext}}(z, \mathbf{r}_{\perp}|M_1) \rangle, \quad (6)$$

where \mathbf{r}_{\perp} is the 2D position vector transverse to the line of sight, and L is the slab thickness. For convenience, we have taken the center of halo M_1 to be at half the slab's thickness. Combining the above expressions, we can write the last equation as a sum of contributions from uniformly-distributed matter, uncorrelated with the cluster M_1 , and from clustered matter, correlated with the halo:

$$\langle M_{\text{ext}}(M_1) \rangle = \langle M_{\text{uni}}(M_1) \rangle + \langle M_{\text{corr}}(M_1) \rangle. \quad (7)$$

To predict the change in the mass of a projected peak due to both these terms, we need to convolve Eq. (6) with a filter, that we shall generically denote by W :

$$\langle M_{\text{uni}}(M_1) \rangle = 2 \rho_m \int d^2 r_{\perp} W(\mathbf{r}_{\perp}) \int_{\sqrt{R_{\text{vir}}(M_1)^2 - r_{\perp}^2}}^{L/2} dz; \quad (8)$$

$$\begin{aligned} \langle M_{\text{corr}}(M_1) \rangle &= 2b(M_1) \int dM_2 M_2 b(M_2) n(M_2) \\ &\times \int \frac{dk}{2\pi^2} k^2 U(k, M_2) P(k) \int d^2 r_{\perp} W(\mathbf{r}_{\perp}) \\ &\times \int_{\sqrt{R_{\text{vir}}(M_1)^2 - r_{\perp}^2}}^{L/2} dz j_0(k \sqrt{r_{\perp}^2 + z^2}), \end{aligned} \quad (9)$$

where ρ_m is the mean matter density of the Universe. W is a dimensionless function, so the right-hand side members of the above equations have mass dimension. If W is a compensated filter (see section § IV) then the right-hand side of Eq. (8) is very small and negative; it would be in fact zero but for the dependence on r_{\perp} of the lower limit of the line-of-sight integral. Throughout this analysis we are using a compensated filter, so we shall drop the contribution of $\langle M_{\text{uni}} \rangle$ since it is tiny compared to $\langle M_{\text{corr}} \rangle$. Note that an upper bound for the magnitude of the impact of correlated projections can be obtained if one takes the lower limit of the line-of-sight integral in Eq. (9) to be 0, and the slab thickness to be infinite. In that case, only the modes transverse to the line of sight contribute to $\langle M_{\text{corr}} \rangle$ and one can rewrite Eq. (9) in the following way:

$$\begin{aligned} \langle M_{\text{corr}}^{\text{max}}(M_1) \rangle &= b(M_1) \int dM_2 M_2 b(M_2) n(M_2) \\ &\times \int dk_{\perp} k_{\perp} U(k_{\perp}, M_2) P(k_{\perp}) \\ &\times \int_0^{R_{\text{vir}}} dr_{\perp} r_{\perp} W(r_{\perp}) J_0(k_{\perp} r_{\perp}), \end{aligned} \quad (10)$$

where J_0 is the zero-order Bessel function. To illustrate the mass change induced by correlated projections on 3D NFW halos, we have estimated Eq. (9) in two cases: a top-hat filter, and a compensated, NFW-shaped filter that we describe in §IV and that we used for the entire study. The limits of the k -integral were adjusted to match the volume of our simulations. For the top-hat

filter, Eq. (9) can be written as:

$$\langle M_{\text{corr}}(M_1) \rangle = 2b(M_1)\rho_m \int_0^\infty dk P(k) \times \int_{R_{\text{vir}}(M_1)}^{L/2} dz \left[\cos(kz) - \cos(k\sqrt{R_{\text{vir}}(M_1) + z^2}) \right]. \quad (11)$$

Here we have taken $U(k, M_2) \approx 1$; the integral over M_2 was then evaluated directly, giving ρ_m .

Figure 1 shows the change in mass arising from correlated projections in a $51 h^{-1}$ Mpc slab as a function of the virial mass of halos. The top-hat results are represented with green empty circles, while the red stars correspond to the compensated filter that we use throughout this work. The blue triangles are the upper limit contribution given by Eq. (10), and computed with the compensated filter. The message of the figure is that the filter choice is crucial in reducing the impact of correlated projections on the measured peaks: the change in mass is ≈ 8 times larger for the top-hat filter than for the compensated, NFW filter. This is due to the fact that the latter is very sensitive to cluster-scale modes, and less so to the larger-scale modes which give rise to projections.

IV. FILTERING THE PROJECTED DENSITY FIELD

In this section we present the filter with which we convolve the density field, similar to that described in Mariani and Bernstein [21]. We used this filter in section §III to estimate the halo-model prediction of the mass change induced by correlated projections. Every point of the filtered density map has an associated mass given by:

$$M(\mathbf{x}_0) = \int d^2x W(\mathbf{x}_0 - \mathbf{x})\Sigma(\mathbf{x}), \quad (12)$$

where W is the filter function and Σ denotes the projected density of dark matter. The filter is compensated [31], i.e. it vanishes when integrated over the aperture size. This ensures that no uniform mass sheet contributes to the measured projected density:

$$\int_0^R d^2x W(\mathbf{x}) = 0, \quad (13)$$

where R is the aperture radius. The filter is also optimal, i.e. maximizes the signal-to-noise (S/N), and it is tuned to NFW clusters: an overdensity with the NFW density profile is detected with a maximum S/N . Although the profile of the halos best recovered by the filter is NFW, the mass is that defined by ST, i.e. an enclosed overdensity threshold $\rho = \Delta_{\text{vir}} \rho_m$ as opposed to $\Delta_{\text{vir}} \rho_{\text{crit}}$. Here ρ_m is the mean matter density, ρ_{crit} is the critical density, and $\rho_m = \Omega_m \rho_{\text{crit}}$. $\Delta_{\text{vir}} = 200$ for ST and NFW. Thus, in the Λ CDM model, ST and NFW clusters have the same density profile, but ST halos have a larger cut-off radii

and concentration parameters than NFW ones. The filter is normalized to ST virial masses in order to facilitate the comparison of the 2D peaks with the 3D halos of our simulations, and also with the ST mass function. There is an agreement of $\approx 10 - 20\%$ between the FoF and the ST mass functions. As shown in numerous earlier studies [21, 23, 31], W is an optimal filter if it is proportional to the expected measured signal and inverse proportional to the variance of the noise. If the observable is the convergence field (or in this case the projected density field), Schneider [31] has shown that W is optimal and compensated, if it has the form:

$$W(\mathbf{x}) = \mathcal{C}_W (\Sigma_{\text{ST}}(\mathbf{x}) - \bar{\Sigma}_{\text{ST}}(R)), \quad (14)$$

with the mean density inside the aperture radius R defined by: $\bar{\Sigma}(R) = 2/R^2 \int_0^R dx x \Sigma(x)$. We determine the normalization constant \mathcal{C}_W from the conditions that the filter be tuned to the NFW profile and return the ST virial mass:

$$\mathcal{C}_W = \frac{M_{\text{vir}}^{\text{ST}}}{\int d^2x |\Sigma_{\text{ST}}(\mathbf{x})|^2 - \pi R_{\text{vir}}^2 \bar{\Sigma}_{\text{ST}}^2(R)}. \quad (15)$$

We choose the aperture radius R to be the virial radius associated with an ST cluster of mass $M_{\text{vir}}^{\text{ST}}$, i.e. $M_{\text{vir}}^{\text{ST}} = 4\pi \Delta_{\text{vir}} \rho_m R_{\text{vir}}^3/3$. Σ_{ST} is the truncated ST projected density:

$$\Sigma_{\text{ST}}(x) = 2r_s \delta_c^{\text{ST}} \rho_m f_{\text{ST}}(x).$$

r_s is the scale radius of the cluster. The characteristic overdensity of the profile, δ_c^{ST} , is related to the concentration parameter c_{ST} by the condition that the mean density within R_{vir} should be $\Delta_{\text{vir}} \rho_m$:

$$\delta_c^{\text{ST}} = \Delta_{\text{vir}} c_{\text{ST}}^3 / (3 [\log(1 + c_{\text{ST}}) - c_{\text{ST}}/(1 + c_{\text{ST}})]).$$

Finally, f_{ST} is a function which depends on cosmology only through the concentration parameter, see for instance Hamana *et al.* [11]. Its expression varies depending on whether it is evaluated at $r < r_s$, $r = r_s$, $r_s < r < R_{\text{vir}}$, and $r > R_{\text{vir}}$:

$$f_{\text{ST}}(\xi) = \begin{cases} -\frac{(c_{\text{ST}}^2 - \xi^2)^{1/2}}{(1 - \xi^2)(1 + c_{\text{ST}})} + \frac{\cosh^{-1}\left(\frac{\xi^2 + c_{\text{ST}}}{\xi(1 + c_{\text{ST}})}\right)}{(1 - \xi^2)^{3/2}}, & r < r_s \\ \frac{(c_{\text{ST}}^2 - 1)^{1/2}}{3(1 + c_{\text{ST}})} \left(1 + \frac{1}{1 + c_{\text{ST}}}\right), & r = r_s \\ -\frac{(c_{\text{ST}}^2 - \xi^2)^{1/2}}{(1 - \xi^2)(1 + c_{\text{ST}})} - \frac{\cos^{-1}\left(\frac{\xi^2 + c_{\text{ST}}}{\xi(1 + c_{\text{ST}})}\right)}{(\xi^2 - 1)^{3/2}}, & r_s < r < R_{\text{vir}} \\ 0, & r > R_{\text{vir}} \end{cases} \quad (16)$$

Here ξ is dimensionless, $\xi = r/r_s$. The concentration parameter is a function of the halo redshift and mass; we have followed the prescription of Bullock *et al.* [3] to compute it and used the method of Smith and Watts [37] to map $c_{\text{NFW}} \rightarrow c_{\text{ST}}$. The projected density field

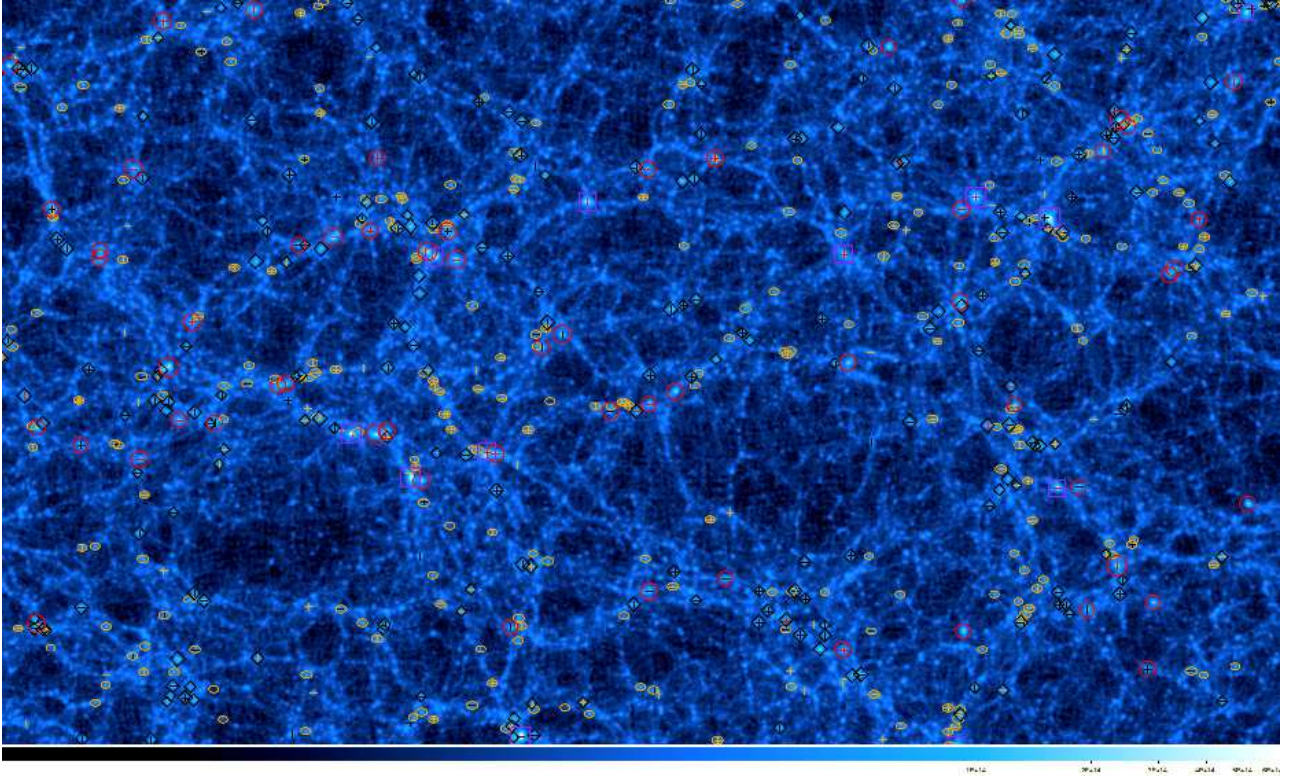


FIG. 2: The filtered projected density field of a $51 h^{-1}$ Mpc slab in the fiducial cosmology. The scale is $512 \times 280 h^{-1}$ Mpc. The detected peaks and FoF halos are marked with colored symbols depending on their mass range. An enlarged snapshot of this image is shown in Figure 4.

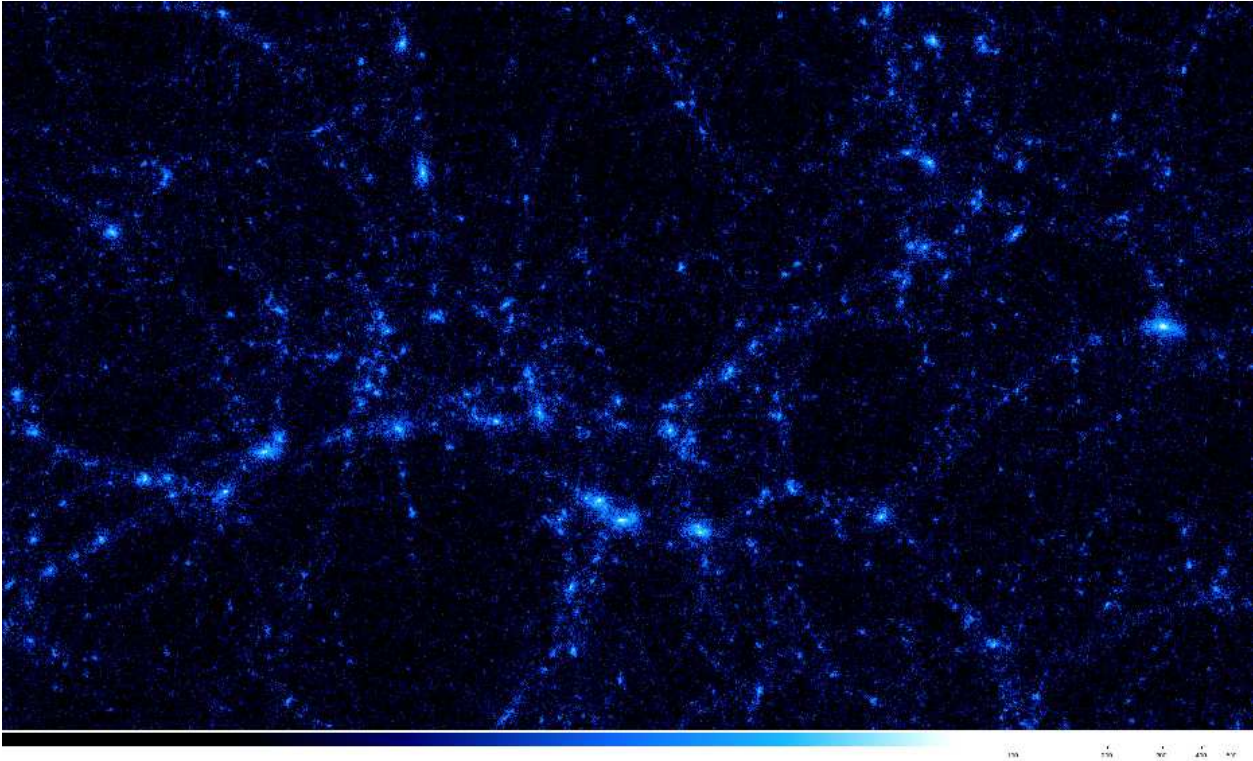


FIG. 3: The unfiltered projected density of the same $51 h^{-1}$ Mpc slab shown in Figure 2. The scale of the picture is $130 \times 70 h^{-1}$ Mpc.

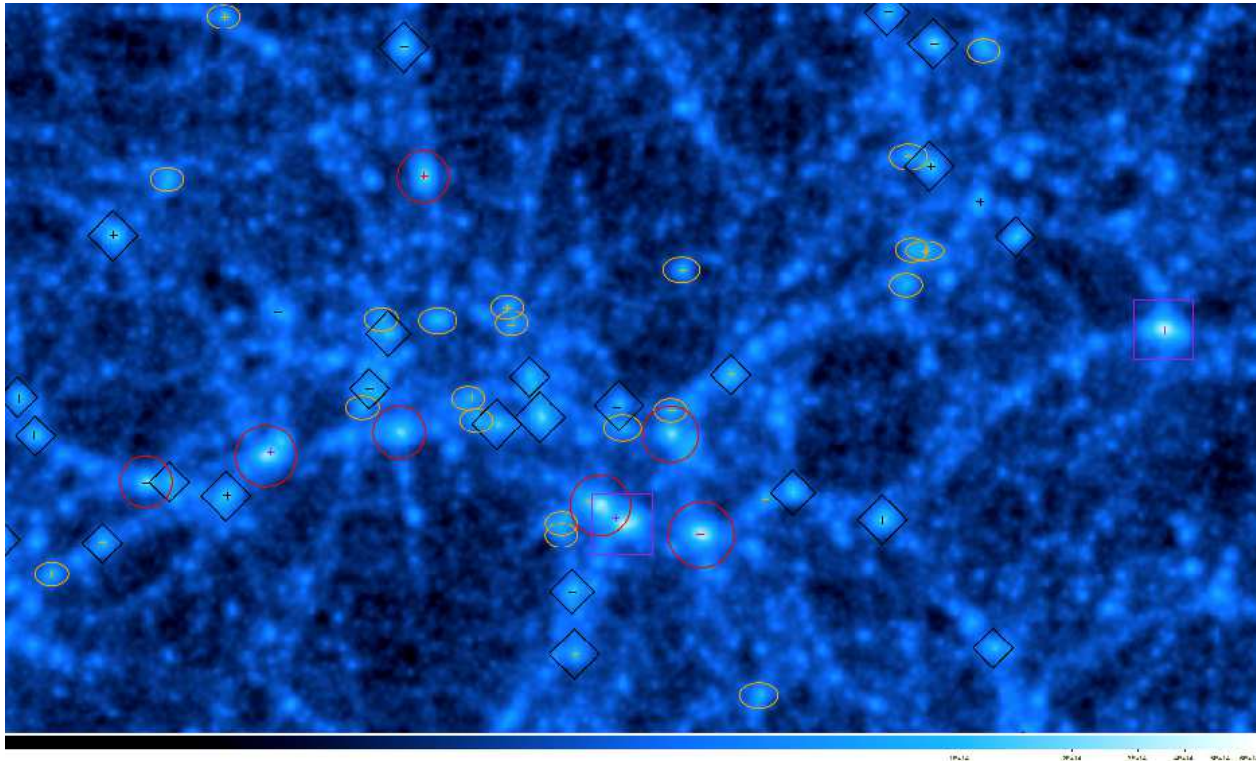


FIG. 4: Same snapshot as above, but this time the projected density field is filtered. The detected peaks are marked with colored symbols depending on their mass range: purple squares for $M > 5 \times 10^{14} h^{-1} M_{\odot}$; red circles for $5 \times 10^{14} h^{-1} M_{\odot} > M > 2 \times 10^{14} h^{-1} M_{\odot}$; black rombs for $2 \times 10^{14} h^{-1} M_{\odot} > M > 8 \times 10^{13} h^{-1} M_{\odot}$; and orange ellipses for $8 \times 10^{13} h^{-1} M_{\odot} > M > 5 \times 10^{13} h^{-1} M_{\odot}$. The FoF halos are represented with crosses and the color choice for each mass range is the same as for the peaks. The scale of the picture is $130 \times 70 h^{-1} \text{Mpc}$.

smoothed with the filter (14) matched to a cluster of mass $M_{\text{vir}}^{\text{ST}}$ will yield a maximum signal at the location of an ST cluster center, which we denote as $M(\mathbf{x}_0 | M_{\text{vir}}^{\text{ST}})$. If the cluster's mass were that of the filter, then the amplitude of the smoothed field at the peak would be:

$$M(\mathbf{x}_0 | M_{\text{vir}}^{\text{ST}}) = M_{\text{vir}}^{\text{ST}}. \quad (17)$$

In practice, in order to assign a mass to a cluster, we apply several filters of different masses, and interpolate to find the mass $M_{\text{vir}}^{\text{ST}}$ at which (17) would be satisfied. This is the mass assigned to the peak.

V. A HIERARCHICAL PEAK FINDING ALGORITHM

As stated earlier, our observable is the projected density field of dark matter, and our goal is to study the effect of correlated projections on the 2D-peak mass function. We divide the simulation cube in several numbers of slabs of equal thickness: 20 (slabs of approximately $26 h^{-1} \text{Mpc}$), 10 ($\approx 51 h^{-1} \text{Mpc}$), 5 ($\approx 102 h^{-1} \text{Mpc}$), 2 ($= 256 h^{-1} \text{Mpc}$), and 1 ($= 512 h^{-1} \text{Mpc}$). Each set of equal slabs is analyzed separately, i.e. the projected density field is filtered, and peaks are identified as the highest

maxima in the filtered map. A selection algorithm is then applied to decide on the validity and on the final mass of these peaks.

One distinguishing feature of our method is that we filter the density maps recursively, with a hierarchy of matched filters. The shape of the matched filter depends upon the mass $M_{\text{vir}}^{\text{ST}}$ of the cluster one is attempting to detect. We start with the highest-mass filter, convolve it with the map, and find all peaks above the target mass. We repeat the procedure for lower mass filters. Peaks that have been already found with a higher mass filter are discarded. Thus, we do not face the problem of 'halos-in-halos' (Hamana *et al.* [11]). The last filter applied corresponds to the detection threshold of $5 \times 10^{13} h^{-1} M_{\odot}$. Below this threshold, the mass resolution of the simulations affects the filter efficiency, as shown in the next section. To the identified peaks we associate a virial radius given by $R_{\text{vir}} = (3M_{\text{vir}}^{\text{ST}}/4\pi\Delta_{\text{vir}}\rho_{\text{m}})^{1/3}$, as described in the previous section. If two peaks have distinct centers (i.e. $\hat{x} - \hat{y}$ coordinates), but overlapping radii of the same size, we keep both peaks. If the centers are distinct, but one of the peaks has a smaller radius than the other one, and it is therefore 'enclosed' in the projected disk of the larger peak, we keep the higher-mass peak and discard the lower-mass one. Figures 2, 3, and 4 show filtered and unfiltered maps of one of the slabs of the fiducial

cosmology. Figure 2 presents a filtered slab, with the detected peaks and FoF halos marked on the filamentary structure of the projected density field. Figure 3 is a zoom-in of the same slab, before filtering, and Figure 4 is a zoom-in after filtering. In the latter, FoF halos are marked by crosses of different colors, according to the mass range where they belong, while peaks are marked by symbols of various shapes and colors – see the caption for the mass legend.

A nontrivial issue regarding the slabs is that of the peaks which are situated right on the boundary of two slabs and are therefore split in two. The consequence of such a boundary split is that the peak is detected in neither slab or, even if it is detected in one of them, its filter-associated mass is significantly reduced compared to the true value. On average, in a $50 h^{-1}$ Mpc slab, about 20% of the peaks suffer from boundary-split effects. We addressed this problem by considering two sets of slabs: ‘normal’, and ‘interlaced’ slabs. Compared to the normal slabs, the interlaced ones are shifted by half a slab thickness on the axis of projection. Thus, the boundary of two normal adjacent slabs goes right through the middle of an interlaced slab, so that halos that are divided in the normal slabs appear whole in the interlaced slabs, and vice versa. We analyze the peaks in both sets of slabs and compare them based on their location in the $\hat{x} - \hat{y}$ plane (we consider the projection axis as the \hat{z} direction), and their filter-associated mass. To be precise, the peaks in every normal slab are compared to those in the two adjacent interlaced slabs which contain the normal slab. The peaks in every interlaced slab are also compared to those in the two adjacent normal slabs which contain the interlaced slab. If we find peaks with the same or nearly the same $\hat{x} - \hat{y}$ coordinates, but with masses that differ by more than 5%, we consider that we have a boundary split case and select the peak that has the higher mass. If the difference in mass is smaller than 5%, we keep the original masses.

Halos often ‘live’ in filaments; if the filaments are oriented along the projection axis, they can contribute to the mass of peaks sourced by the respective halos, or they can even form peaks of their own. Even when a halo is not right on a slab boundary, but it is close to it, its filament can extend beyond the boundary. By splitting the filament, the projected mass of the halo is slightly decreased. The 5% threshold mentioned above not only removes the problem of split halos, but it also makes split filaments less likely. For the thickest slab with potential boundary problems, i.e. $256 h^{-1}$ Mpc, we use a higher threshold of 15%, in order to avoid biasing our mass measurements to higher masses. In this case there is only one boundary, and hence fewer split objects.

VI. TESTING THE FILTER

A. Numerical tests of the filter

The filter described earlier is optimal in the ideal conditions of infinite particle-mass resolution. The fact that the simulation halos have a discrete mass distribution changes the performance of any filter when applied to simulation data. Also, our filter is tuned to spherically symmetric halos, but real halos are more triaxial than spherical. We have investigated the efficiency of our filter in two idealized cases: first, on synthetic NFW halos, to understand the effects of the finite mass and mesh resolutions; second, on isolated FoF halos (that is, only the particles from a single halo) of our simulations, to see the effects of the halo asphericity. Both tests were carried out for the fiducial cosmological model, as there is no reason to assume that such numerical effects would manifest themselves differently in the variational cosmologies.

The synthetic NFW halos that we have generated have the same mass resolution as our simulations. The particles are sampled in the radial direction with the NFW density profile, and their angular distribution is uniform random on the sphere. The tests were performed for 3 different masses, using an ensemble of 1000 synthetic halos for each mass. We found that the finite particle mass resolution mostly affects the signal in the inner region of the clusters, defined by the scale radius. That is because the NFW density profile has a significant fraction of its mass enclosed within the scale radius ($\approx 20\%$). Given the mass resolution of our simulations, the inner region of average clusters is poorly populated with particles, and actually unresolved for radii smaller than the softening length of the simulations ($60 h^{-1}$ kpc, in our case). Therefore, we have chosen to ‘core’ the ST profile, i.e. we consider the density profile of the filter to be constant for a radius $< r_{\text{core}}$:

$$\Sigma_{\text{ST}}(r) = \begin{cases} \Sigma_{\text{ST}}(r_{\text{core}}), & r \leq r_{\text{core}} \\ \Sigma_{\text{ST}}(r), & r > r_{\text{core}} \end{cases} \quad (18)$$

Thus, the traditional central cusp of the ST profile has been removed from the filter, and the signal of the filtered halos is redistributed so that the outer layers contribute more to it. Even if our simulations had allowed us to use the ST profile without removing its cusp, there is a more physical reason that justifies our choice. Halos relevant to WL surveys have an Einstein radius which is only 2-3 times smaller than the scale radius. Since we are interested in the WL regime, the measured signals of the halos must come from regions well outside the Einstein radius, or else the WL approximation breaks down. Note that the filtered density will be estimated from real data by applying a corresponding filter to the shear map. The shear filter corresponding to our constant-core ST profile has a ‘hole’, i.e. discards the signal coming from within the core radius. This is necessary in practice since it is very difficult to measure the shear around clusters

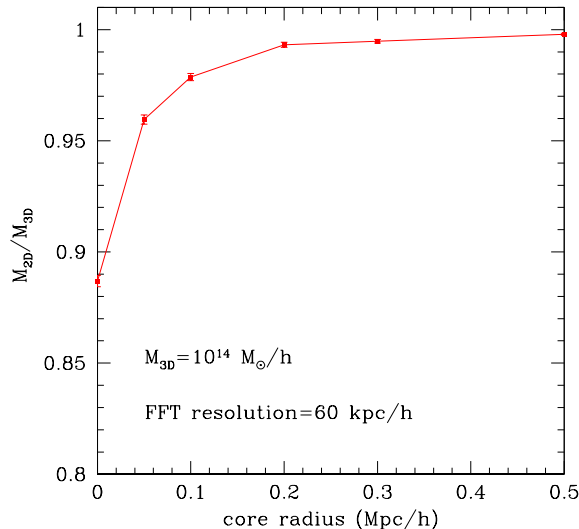


FIG. 5: The dependence of the filter efficiency on the core radius, for the Fourier mesh used throughout the paper ($60 h^{-1}$ kpc). The efficiency is defined as M_{2D}/M_{3D} , where M_{3D} is the Sheth-Tormen virial mass of the synthetic halo, and M_{2D} is the mass of the projected peak, assigned as described in §IV. We show the average of measurements of 1000 projected synthetic Sheth-Tormen halos, in the fiducial cosmology. We chose a core radius of $200 h^{-1}$ kpc to perform our analysis.

at small radii from the center: most shear measurement methodologies fail in regions of strong lensing, and cluster member galaxies often obscure the lensed background galaxies.

Figure 5 plots the dependence of the filter efficiency – defined as M_{2D}/M_{3D} – on the filter core radius for an ensemble of synthetic halos of mass $10^{14} h^{-1} M_{\odot}$. M_{2D} is the mass that we assign to the density peaks in the way described in section §IV, and M_{3D} is simply the ST virial mass of the synthetic halos. The figure clearly shows the filter efficiency to be $\approx 90\%$ even for halos obeying perfectly the NFW profile, if no coring is done. Though not shown in the figure, we have also probed that the efficiency would be more than 95% if the mass of the simulation particles were lower by a factor of 10, with no core applied. However, since this mass resolution is not available, throughout this study we have adopted a core value of $200 h^{-1}$ kpc. This is also valid for the results published in Marian *et al.* [22].

Equation (12) is a real space convolution. By smoothing the density field of dark matter with a filter, we expect to erase the structure on scales smaller than the scale of the filter. It is convenient to do the smoothing in Fourier space, and in order to compute the discrete Fourier transform of the density field, we project it on a grid. We refer to the ratio of the simulation cube side L and the number of grid points taken on that side, as

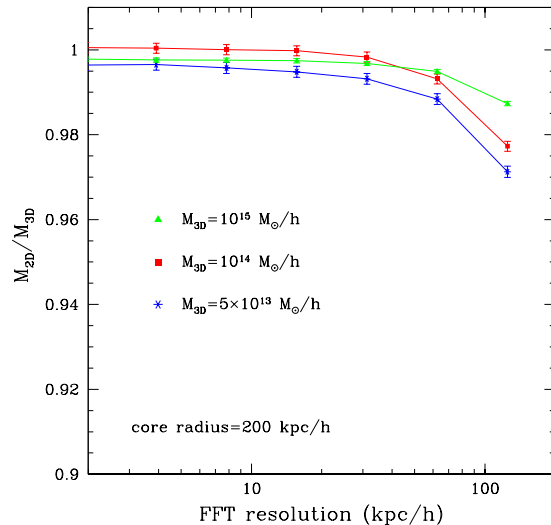


FIG. 6: The dependence of the filter efficiency on the Fourier mesh, for a core radius of $200 h^{-1}$ kpc. The filter efficiency is defined as in Figure 5. For each mass we plot the average of the measurements of 1000 synthetic Sheth-Tormen halos in the fiducial cosmology. Throughout our analysis, we used a mesh of $60 h^{-1}$ kpc.

the Fourier mesh resolution. Our whole analysis of the simulation data was done with a mesh resolution of $60 h^{-1}$ kpc. In Figure 6 we plot the filter efficiency dependence on the Fourier mesh resolution for the chosen core value. Large halos are less affected than small halos by resolution effects, and in general the filter efficiency is of about 98% for our mesh and core chosen values. Since we do not wish to include in our analysis halos that are too small and too ‘poor’ in particles, we have imposed a mass detection threshold of $5 \times 10^{13} h^{-1} M_{\odot}$ for the projected peaks. We do not include in our analysis peaks with mass below this threshold.

Figure 7 shows the correspondence of FoF masses and 2D masses recovered by our filter, *in the absence* of projections. The FoF halos have been projected by themselves: only the particles identified by the halo finder as being part of a halo have been projected. Again, the efficiency is defined as M_{2D}/M_{3D} : M_{2D} is the mass assigned to the density peaks according to section §IV, and M_{3D} is the FoF mass of the simulation halos that we analyze. The filter efficiency is depicted for 3 large mass bins. The FoF halos were selected from all eight realizations of the fiducial cosmology. The plot reveals that the vast majority of the FoF halos are shifted to lower masses by our filter. This is mostly due to departures of the halo density profiles from the spherically symmetric NFW profile: the filter given by Eq. (14) is a spherical overdensity (SO)

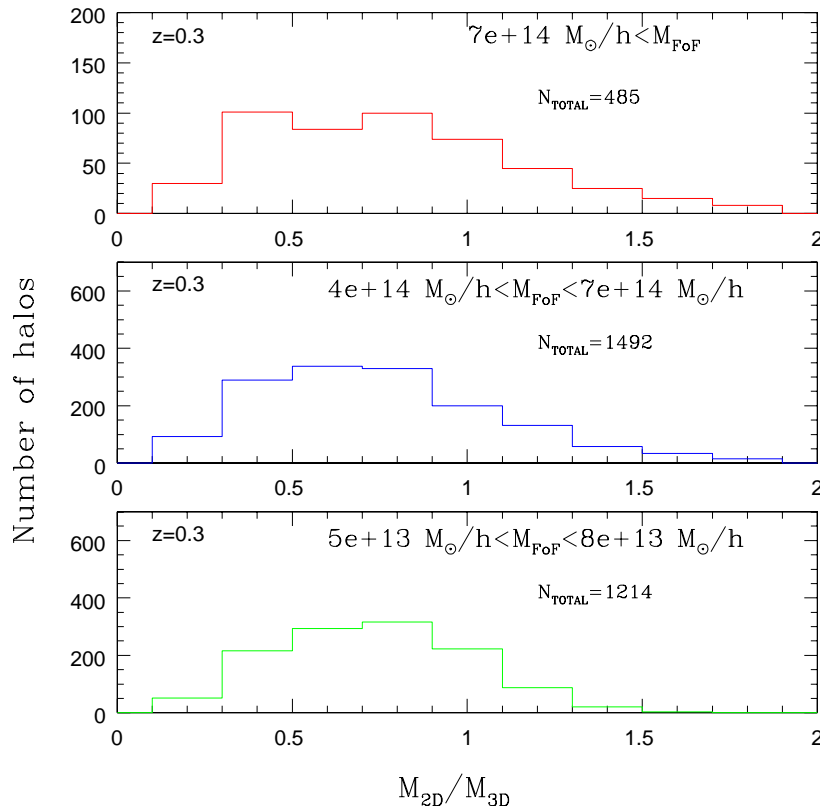


FIG. 7: The filter efficiency in the absence of projections. M_{3D} is the FoF mass of the simulation halos, and M_{2D} is the mass of the peaks obtained by projecting the FoF halos by themselves, i.e. only the particles forming them. Three FoF mass bins are considered, with the total number of halos per bin indicated in the figure. We attribute the shift towards lower masses to departures of the FoF halos from the spherically-symmetric NFW profile. The dispersion in the recovered mass decreases for the bins of lower mass, in accord with the fact that the largest halos are the most triaxial ones.

filter that we apply to FoF halos. FoF and SO masses are known to differ. Indeed, had we applied an SO 3D halo finder, or had we used another FoF linking length, the filtered masses would have had a different distribution and mapping to the 3D halos. It is also possible that the scatter in the concentration parameter, which is well known to be described by a log-normal distribution (Bullock *et al.* [3]) might also cause some of the scatter seen in Figure 7. Also, halos have substructures, e.g. [26]. Since we are interested in the cosmology scaling of the projected-peak mass function, and not in the analysis of individual clusters, the mapping between FoF halo masses and filtered masses is not, in this study, of great significance to us. After all, there is no absolute way to define a halo mass. It is worth emphasizing that, unlike Metzler *et al.* [25] and Clowe *et al.* [4] our recovered 2D masses are not the result of averaging projections of the same clusters along different lines of sight. The halos are projected on the same axis as the simulation cubes, and to each of them we apply our filter ‘blindly’, i.e. without assuming any prior knowledge of the true position of the

cluster center. This is valid for our whole analysis. Had our individual cluster mass estimates been an average over several lines of sight, we expect to have found a reduced scatter and a smaller skewness in the distributions shown in Figure 7.

Figure 8 shows the correspondence of FoF masses and 2D masses in the *presence* of projections. Here we have matched the FoF halos of the simulations with the peaks projected in slabs of various thickness. The different colors indicate the thickness of the projection slabs. The binning of the FoF masses is finer than in the previous figure. The sharp cut-off visible in the right lowest panels stems from our selection of peaks larger than $5 \times 10^{13} h^{-1} M_{\odot}$. The halos sourcing these peaks can however have masses lower than this threshold. Not surprisingly, the same trend present in Figure 7 is also visible here. Again the FoF halos are shifted towards lower masses, and the distribution of peaks is non-gaussian. A log-normal distribution fits some of the intermediate mass bins. The slab thickness does not seem to play a significant role in shaping the distribution. While in

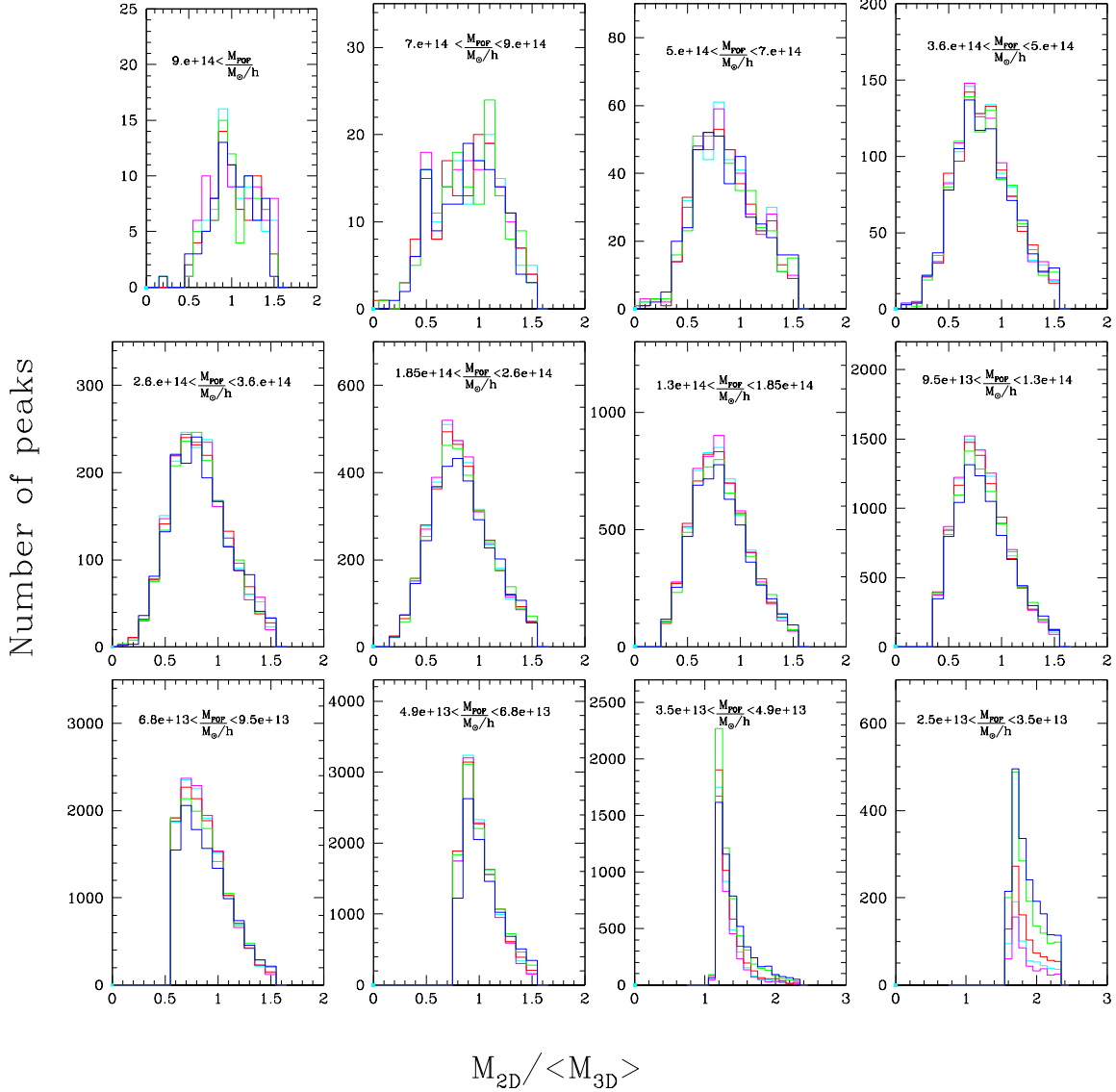


FIG. 8: The filter efficiency in the presence of projections. The efficiency is defined as M_{2D}/M_{3D} , where M_{3D} is the mass of the FoF halos that source the peaks measured in different slabs. M_{2D} is the mass of the peaks formed by the FoF halos, when projected together with the rest of the matter in the slabs: $26 h^{-1} \text{ Mpc}$ – magenta –, $51 h^{-1} \text{ Mpc}$ – cyan –, $102 h^{-1} \text{ Mpc}$ – red –, $256 h^{-1} \text{ Mpc}$ – green –, $512 h^{-1} \text{ Mpc}$ – blue. The distribution is non-gaussian, and the spread is mostly due to departures of the 3D halos from the spherically-symmetric NFW profile.

this study Figure 8 is just illustrative, should we wish to predict the projected-peak mass function from the 3D one, we would need the distribution $M_{2D} - M_{3D}$, as suggested by Metzler *et al.* [25]. Figures 7 and 8 serve as a warning against blind comparisons between 3D and 2D quantities, as often seen in the literature. Figure 7 is an example of ‘filter effects’, i.e. scatter between 2D and 3D masses due to different mass definitions and other causes,

but completely unrelated to LSS projections. Figure 8 shows that such filter effects are dominant compared to the correlated projection effect. Unless the 2D and 3D peaks are found with *the same* filter, it is very difficult to measure the impact of correlated projections directly on 3D masses. In order to remove the filter effects shown in Figure 7, one should measure the change in the mass of peaks projected in slabs of different thickness. This is

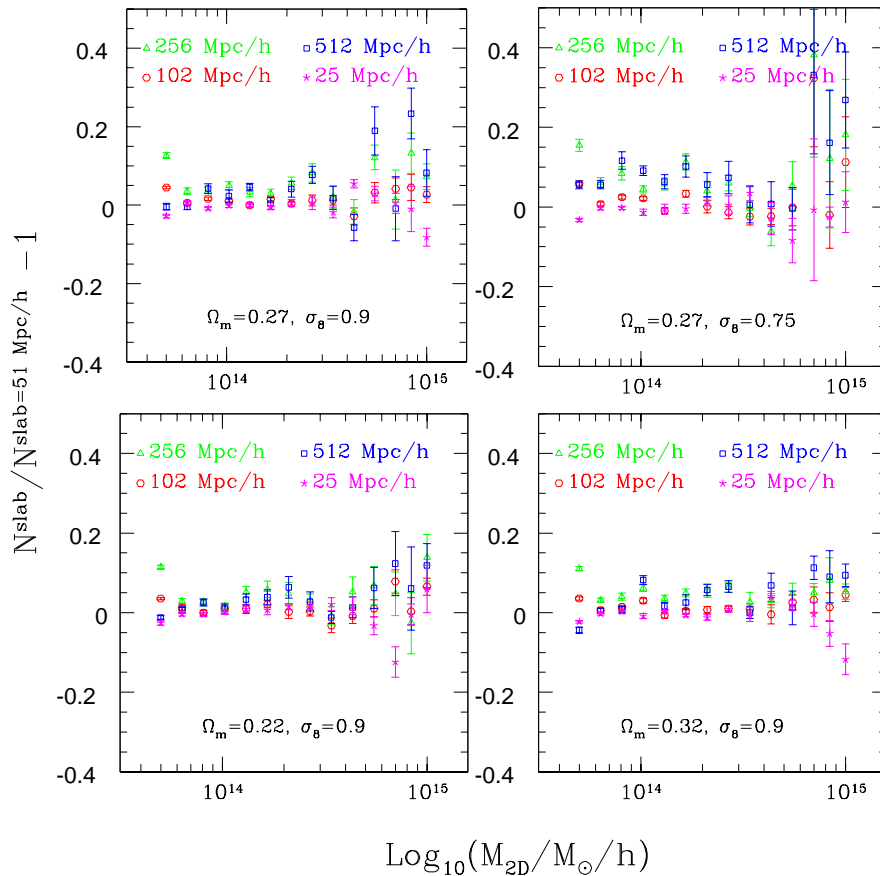


FIG. 9: The fractional difference of the number of projected peaks in slabs of 25, 102, 256, 512 h^{-1} Mpc and the peaks in the fiducial slab of 51 h^{-1} Mpc. Each panel corresponds to one cosmology. The difference in the mass functions for different slabs is due to the correlated projected term described by Eq. (9), as well as to uncorrelated projections in the case of the thickest slabs.

how we proceed in the following sections.

VII. RESULTS

In our previous study Marian *et al.* [22], we analyzed the effect of correlated projections in slabs of 51 h^{-1} Mpc. Here we extend our analysis to several slab thicknesses: 26 h^{-1} Mpc, 102 h^{-1} Mpc, 256 h^{-1} Mpc, and 512 h^{-1} Mpc.

A. Slab thickness tests

First we probe the dependence of the projected density peak abundance on the slab thickness. Figure 9 shows the fractional difference of the peak number counts in the slabs that we investigate, compared to our ‘fiducial’ slab of 51 h^{-1} Mpc. We notice the fractional differences

deviate from 0, particularly at the high-mass end, an anticipated effect of projections. The deviations depend on the slab thickness and also on the cosmological model – the low- σ_8 cosmology shows greater sensitivity to the slab variations than the other three models. We expect the most significant changes from the fiducial slab peak abundance to occur precisely at the high-mass end: there are few high-mass clusters, so a small variation in their mass can alter their distribution on the exponential tail of the mass function considerably. In particular, for the 512 h^{-1} Mpc and even the 256 h^{-1} Mpc slabs, this variation may be increased by the presence of chance projections along the line of sight, which seems to be suggested by Figure 9. The correlation length of large clusters is $\approx 30 h^{-1}$ Mpc, therefore we do not expect correlated projections to affect the abundance of peaks in these slabs. There is also an increase in the high-mass peak abundance corresponding to the fiducial slab compared to the 26 h^{-1} Mpc one, while only a very small rise is visible

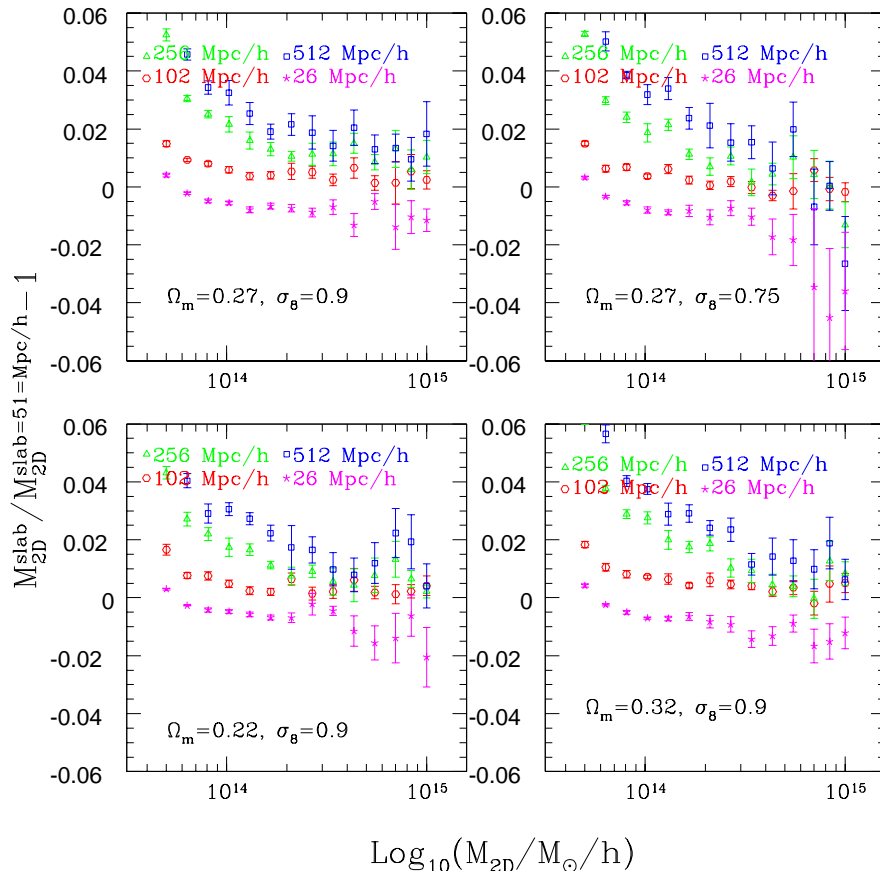


FIG. 10: The fractional change in mass due to correlated projections for peaks measured in different slabs and the fiducial slab peaks. Every peak projected in slabs with the fiducial thickness, was then tracked among the peaks projected in the other slabs.

in the $102 h^{-1}$ Mpc slab compared to the fiducial one—a sign that the correlation function of clusters drops significantly at scales larger than $50 h^{-1}$ Mpc. Overall, we are satisfied with the robustness of the mass function projected in slabs of various thickness: analyzing the projected density field with a compensated filter has rendered the resulting peak abundance largely independent of the slab thickness.

B. The mass change induced by correlated projections on individual peaks

In section §III we used the halo model to predict the change in the projected mass of a cluster induced by structures correlated with it, i.e. Eq. (9). We have evaluated this expression for the particular case of our filter, described by Eq. (14). In this case, Figure 1 indicated that there should be a very small change ($< 2\%$) in the 2D mass of peaks – defined in section §IV –, compared

to their 3D mass – defined as the ST virial mass. In this section we test the halo model prediction. Since our 3D masses have not been identified with an SO filter, but with the FoF algorithm, we cannot probe the result of Eq. (9) directly. Instead, we circumvent this difficulty by comparing only masses of objects identified with the same filter.

First we follow the mass change for the simulation clusters when projected in slabs of various thickness. We have traced every peak in the fiducial slab among the peaks corresponding to the other slabs. We have selected only those peaks that maintained roughly the same $\hat{x} - \hat{y}$ coordinates in all the slabs where they were projected – we did not allow the coordinates to shift by more than $\approx 120 h^{-1}$ kpc. This restriction was imposed to ensure that we compare the mass of *the same* peaks traced in different slabs. Figure 10 presents the fractional change in mass for the peaks projected in the variational slabs compared to the fiducial slab (symbols). The error bars represent errors on the mean of the eight realizations of

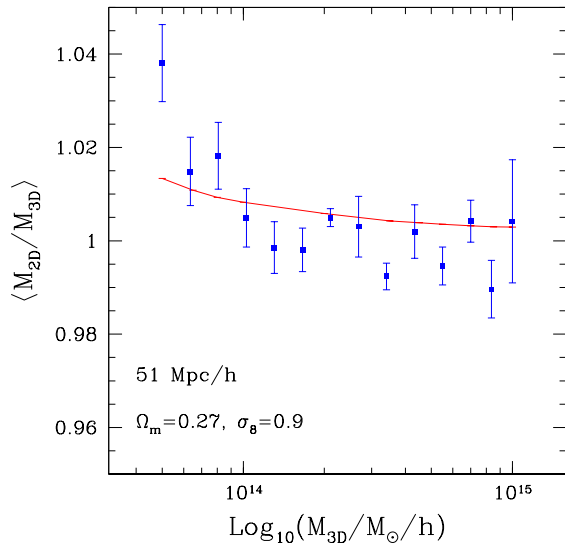


FIG. 11: A test of Eq. (9): M_{3D} is the mass of FoF halos projected by themselves, and filtered according to Eq. (14). M_{2D} is the mass of the peaks sourced by the same FoF halos when projected in slabs of the fiducial thickness, together with all the mass in the respective slabs. The solid line is the halo model prediction from Eq. (9).

each cosmology. We have measurements for all four cosmologies. One remarkable feature may be noted: the simulation data indicate the impact of correlated projections on the measured halo masses to be *very small*, i.e. about 2% for peaks measured in slabs of $26 h^{-1}$ Mpc and $102 h^{-1}$ Mpc relative to the fiducial slab peaks. The exception is the low- σ_8 cosmology, which shows stronger deviations at the high-mass end. The halo model prediction for the change in mass of peaks projected in slabs of $26 h^{-1}$ Mpc and $102 h^{-1}$ Mpc compared to peaks projected in slabs of $51 h^{-1}$ Mpc is that it should be smaller than 0.1%. Figure 10 indicates a more noticeable change, however. The slightly larger measured mass changes (4%) for the two thickest slabs are likely due to chance projections.

Second, we carry out a comparison between peaks measured in slabs of thickness 0 and peaks measured in the fiducial slab. To be precise, we take a large number of the FoF halos (≈ 8000) from the fiducial cosmology, and project only the particles within the halos themselves. An identical procedure was followed to obtain the distribution in Figure 7. In this case, we filter a larger number of halos, and take finer mass bins. We consider the mass of the peaks obtained through the projection of the FoF halos by themselves as a proxy for the 3D ST virial mass. We then compare this mass to the mass of the peaks sourced by the same FoF halos when projected together with all the matter in slabs of the fiducial thickness. We do not expect this approximation to be perfect, but it is the closest measurement we can make

on our data for a direct comparison with the halo model prediction shown in Figure 1. The result is shown in Figure 11. Some caution is necessary when interpreting this figure, as for some of the intermediate mass bins, the ratio M_{2D}/M_{3D} goes below unity. Naturally, this should not be the case. We explain this anomaly by the fact that when an FoF halo is projected together with the structure in which it is embedded, the surrounding matter renders it more homogeneous and the compensated filter may therefore attribute it a smaller mass than when the halo is projected by itself. However, despite this anomaly, Figure 11 should be taken as supportive of the halo model prediction, i.e. Eq. (9). Hence we expect that correlated projections alter the masses of clusters at the percent level, and therefore are not a dominant systematic for WL cluster mass measurements. If there is a projection bias in WL mass determinations, it is more likely due to structures uncorrelated with the main lens.

C. Predicting the projected mass function

We now try to address two of the main objectives of this work: in the context of correlated projections, we examine the behaviour of the 2D mass function and also the possibility to predict this behaviour. In Marian *et al.* [22] we have shown that the scaling with cosmology of the 2D mass function projected in slabs of $51 h^{-1}$ Mpc follows very closely the scaling of the 3D mass function and also that of the semi-analytical ST model.

Figure 12 is similar to Figure 2 from Marian *et al.* [22], but generalizes that result to other slab thicknesses. The figure shows the fractional difference of the peak counts for the variational cosmologies scaled by the fiducial cosmology peak counts (solid points). It also shows the same fractional differences for the 3D FoF mass functions measured from the simulations (open magenta symbols), as well as the ST predictions (solid lines). The error bars are on the mean of the eight realizations of each cosmology, and the cosmic variance between realizations is minimized by the choice of initial conditions mentioned in section §II. The difference in the SO filter and FoF mass definitions is also minimized: we compare 2D peaks with 2D peaks and FoF halos with FoF halos.

We maintain the conclusion of Marian *et al.* [22] regarding the very similar scaling with cosmology of the 2D, 3D, and ST mass functions.

We next try to fit the lensing mass function corresponding to the slab thickness of $26 h^{-1}$ Mpc. We shall assume that the functional form proposed by [36] can be used to describe the projected mass function, but with the parameters of the model recalibrated. The ST mass function is given by:

$$\frac{dn_{\text{ST}}(M)}{d \log M} d \log M = \frac{\rho_m}{M} f_{\text{ST}}(\nu) d\nu, \quad (19)$$

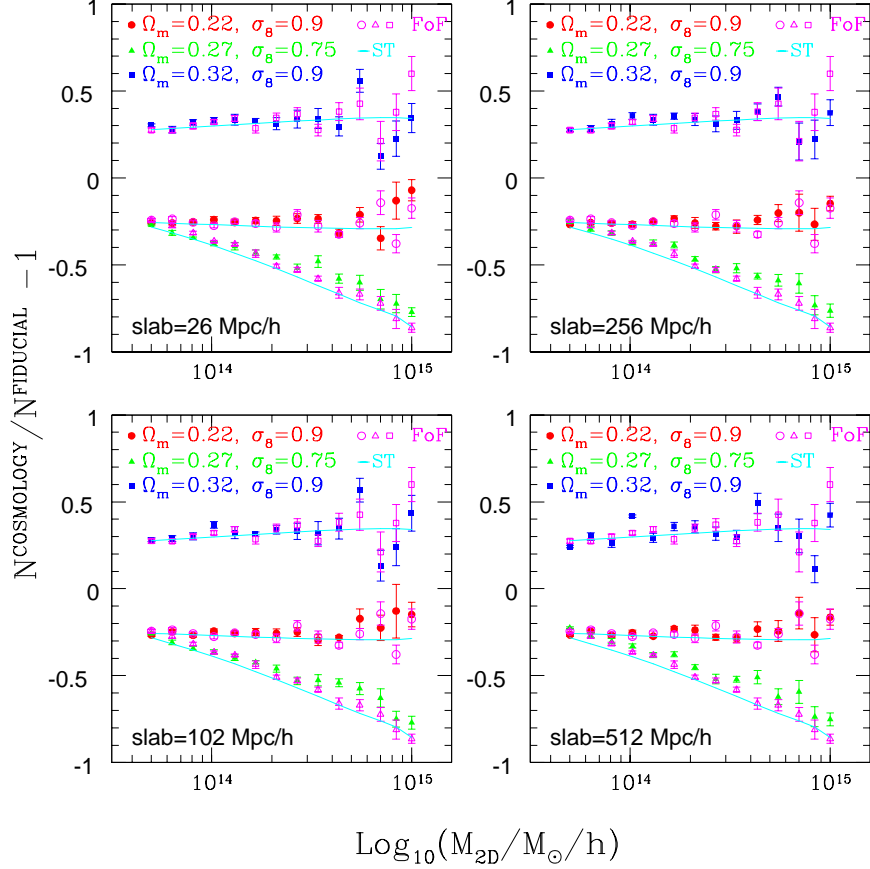


FIG. 12: The mass function of the variational cosmologies, scaled by fiducial cosmology mass function, considering slabs of different thickness. Filled symbols are peak measurements, open ones are FoF halos, and the continuous lines indicate the Sheth-Tormen mass function. The error bars represent errors on the mean of 8 realizations of each cosmology.

with $\nu = \delta_{\text{sc}}^2 / \sigma^2$ and:

$$f_{\text{ST}}(\nu) = A \sqrt{\frac{2a\nu}{\pi}} [1 + (a\nu)^{-p}] \exp(-a\nu/2). \quad (20)$$

In the above $dn_{\text{ST}} = n_{\text{ST}}(M) dM$ gives the number density of halos, σ^2 is the variance of the top-hat-smoothed linear density field, $\delta_{\text{sc}} = 1.69$ is the critical density for spherical collapse. The ST model has two free parameters, with the following values: $a = 0.707$, $p = 0.3$. The normalization parameter A is obtained from the constraint that all mass in the Universe is in halos:

$$\int_0^\infty dM M n_{\text{ST}}(M) = \bar{\rho}. \quad (21)$$

This leads to: $A(p) = [1 + 2^{-p} / \sqrt{\pi} \Gamma(1/2 - p)]^{-1}$. For the ST mass function, $A = 0.3222$. The projected mass function fit conserves this normalization relation, but changes the values of a , p . To fit the parameters we follow the approach of Warren *et al.* [42] and compute the

extended Poisson likelihood for our simulations:

$$\ln \lambda(\mathbf{q}) = - \sum_{j=1}^{N_r} \sum_{i=1}^{N_m} \left[\mu_{ij}(\mathbf{q}) - n_{ij} + n_{ij} \ln \frac{n_{ij}}{\mu_{ij}(\mathbf{q})} \right], \quad (22)$$

where N_r is the number of realizations per cosmology – 8 in our case –, and N_m is the number of mass bins considered. n_{ij} is the measured number of projected peaks in mass bin i of realization j , while μ_{ij} is the predicted number of halos for mass bin i and realization j . We find the point in the parameter space defined by $\mathbf{q}=(a, p)$ which maximizes the above likelihood, and thus we determine the best fit for the projected mass function. Note that, had we been attempting to constrain the mass function at lower masses, we expect that the Poisson model would have not captured the true variance in the distribution, owing to sample variance fluctuations (Crocco *et al.* [6], Hu and Kravtsov [15]).

We have fitted the free parameters for each cosmological model, and our results are the following:

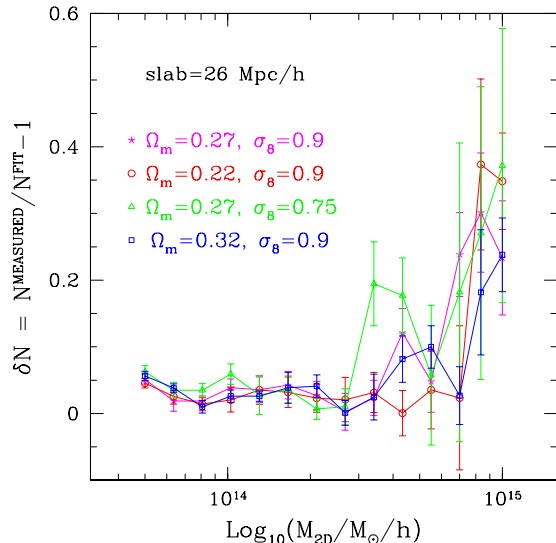


FIG. 13: Fractional difference of measured and fitted 2D mass functions for all four cosmologies. The slab thickness is $26 h^{-1}$ Mpc.

1. Model 1: $a = 0.719$, $p = 0.298$, $A = 0.3242$
2. Model 2: $a = 0.690$, $p = 0.306$, $A = 0.3161$
3. Model 3: $a = 0.665$, $p = 0.318$, $A = 0.3034$
4. Model 4: $a = 0.727$, $p = 0.292$, $A = 0.3301$

Figure 13 shows a comparison between the measured and the fitted projected mass functions for all cosmologies. We note that the ST functional form is not ideal to fit the high-mass end of the 2D peak function: the accuracy of the fits is better than 10% for the low and intermediate mass bins, but drops to 30%-40% for the high mass bins. This is just a consequence of having projection noise added to measurements on a steep mass function. We also try to predict the projected mass functions of the variational models by using only the fit to the fiducial cosmology and ratios of the *standard* ST mass functions:

$$n^X = n_{\text{fit}}^{\text{fiducial}} \times \frac{n_{\text{ST}}^X}{n_{\text{ST}}^{\text{fiducial}}}. \quad (23)$$

In the above, n^X is the predicted 2D mass function for any of the variational cosmologies, $n_{\text{fit}}^{\text{fiducial}}$ is the fit for the 2D mass function of the fiducial cosmology; n_{ST}^X and $n_{\text{ST}}^{\text{fiducial}}$ are the standard ST mass functions for the variational and fiducial cosmologies respectively.

Figure 14 presents the comparison between this prediction and the measured 2D mass functions. The low- and high- Ω_m cosmology mass functions are captured with an accuracy of 10%-20%, at low and intermediate mass bins, while the low- σ_8 model is worse. The modeling fails completely at the high-mass end, which was to be expected

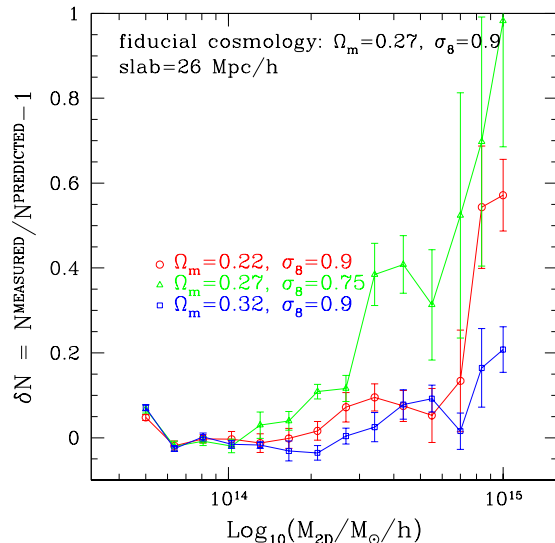


FIG. 14: Fractional difference of the 2D mass function measured in slabs of $26 h^{-1}$ Mpc and the prediction given by Eq (23).

given that for this mass range: (i) there is a large inaccuracy in the fit of the fiducial cosmology; (ii) the ST functional form does not describe well the 2D mass functions of the variational cosmologies either. This simplistic modeling should just be taken as a proof of concept, that the scaling with cosmology of the projected mass function presented in Figure 12 can be used as a starting point for more complicated models of the 2D peak abundance.

VIII. CONCLUSIONS

Future or near-term WL surveys will be able to detect clusters as peaks in shear maps. Projections from LSS are likely to make it difficult to convert the amplitude of the shear peaks to traditionally-defined cluster masses. However, it is possible to circumvent this conversion if the cosmology dependence of the shear-peak counts is understood. In this case, one can constrain cosmology by measuring directly the shear-peak abundance. While this can be done in dark matter simulations, as recently shown by Dietrich and Hartlap [9], it is not practical to rely only on numerical methods. The standard cosmological model contains 6 free parameters, and so the space of models to be tested may quickly become large. Thus, if a well-understood analytical framework can be identified for the peak counts, it will hopefully facilitate an accurate interpolation between expensive numerical predictions made in this high-dimensional space of cosmological models. This is the main motivation for our study.

In this paper we focused attention on estimating and understanding the effect of ‘correlated’ projections on the mass function of density peaks projected in slabs of different thicknesses. We reserve ‘uncorrelated’ projections for future study. Correlated projections are ideally studied in slabs, given the fact that the correlation length of average clusters is $\approx 30 h^{-1}$ Mpc. In such slabs, the projected density is equal to the convergence up to a constant, so it is perfectly adequate to choose it as an observable.

In §II we described the large ensemble of numerical simulations that were generated for our study. These consisted of 4 cosmological models with 8 simulations per model and with total volume per model $V_{\text{tot}} = 1[h^{-1} \text{Gpc}]^3$.

In §III we presented a calculation based on the halo model of structure formation of the expected change in the mass of 3D clusters induced by correlated projections. We showed that the mass increase depends on the filter applied to the projected density field. For a top-hat filter, the increase in mass due to correlated projections is of 10 – 15%. For a matched, optimal, compensated filter, it is roughly a factor of 8 lower. Thus, the halo model predicts that correlated projections should not alter the virial mass of clusters by more than 2%.

In §V we described our algorithm for identifying projected-density peaks. One important new element was that we offered a solution to the problem of ‘peaks-in-peaks’. We did this through applying a hierarchical filtering strategy. We used different scales for the matched filter and took a top-down approach to peak detection. Smaller peaks that were contained within higher mass peaks were discarded.

We have used the same optimal filter as in Marian and Bernstein [21]. This filter is compensated, maximizes the S/N, and matches the NFW density profile. Its normalization is chosen so that it returns the ST virial mass of halos. Tests on synthetic data, i.e. perfect NFW halos, have shown in section §VIA that the filter requires ‘coring’ when applied to simulated data, due to the finite mass and mesh resolutions. The coring will also be necessary for application to real WL measurements, due to practical difficulties of making precise WL measurements in the inner regions of galaxy clusters.

We have measured the distribution $M_{2\text{D}}/M_{3\text{D}}$ – where $M_{3\text{D}} = M_{\text{FoF}}$ – in the presence of projections: we have matched the FoF halos of the simulations and the peaks measured from the density field projected in slabs of different thickness. We have found this distribution scattered and biased towards values smaller than 1. We have also measured the same distribution in the absence of projections, by projecting the FoF halos by themselves. Even in this case the distribution $M_{2\text{D}}/M_{3\text{D}}$ was scattered and biased towards values smaller than 1. This shows that most of the scatter between $M_{2\text{D}}$ and $M_{3\text{D}}$ is not due to LSS projections, but rather to the departures of the FoF halos from the spherically-symmetric NFW profile, to the existence of substructures, and possibly to the scatter and stochasticity of the concentration param-

eter.

The point of these tests is to clarify a somewhat loose perception in the literature concerning the impact of LSS projections on cluster mass measurements: when comparing 2D versus 3D quantities (i.e. mass, S/N, etc.), one must account for the halo/cluster identification algorithms. The scatter in the relation between SO and FoF-identified halos is sure to confuse the interpretation of LSS projections, and can lead to an overestimation of the latter. Since we were unable to apply our matched filter algorithm in 3D (we used a 8192^2 FFT in 2D, and so would require a 8192^3 FFT in 3D), we avoided the confusion of SO-FoF by examining the change induced by correlated projections in density peaks projected in slabs of various thicknesses.

In §VII we measured the projected-peak function in slabs of 26, 51, 102, 256, 512 h^{-1} Mpc. The use of the compensated filter rendered the 2D mass function quite stable with the slab thickness. We then measured the mass evolution of peaks when projected in the different slabs. We found that the average change in mass of peaks measured in slabs of 26 h^{-1} Mpc and 102 h^{-1} Mpc, compared to their mass in the 51 h^{-1} Mpc slab, is no greater than 2%. For the thicker slabs of 256 h^{-1} Mpc and 512 h^{-1} Mpc, the average change is also less than 4%; we expect these thicker slabs to be affected by uncorrelated projections. The halo model suggests that a peak measured in a 51 h^{-1} Mpc slab should suffer a change in mass smaller than 0.1% compared to when it is measured in a 26 h^{-1} Mpc slab. So these changes are larger than the halo model predictions. On the other hand, we have tested that the absolute change in the mass of halos is also at the percent level, in accord with the halo model results. Let us emphasize that all these findings depend on the choice of filter: our filter reduces dramatically the impact of correlated projections compared to other filters. The importance of the filter function in reducing the LSS contamination of WL cluster mass measurements was first suggested by Maturi *et al.* [23]. We conclude that with a proper choice of filter, correlated projections are not a major contaminant for WL-cluster mass measurements. Uncorrelated projections are likely to be the dominant contributor to the projection bias.

We also confirm the main result of our earlier study Marian *et al.* [22]: the projected peak abundance has the same scaling with cosmology as the 3D and ST mass functions. This is valid for all the slab thicknesses that we probed. We proposed a very simple fitting procedure for the 2D mass function, adopting the functional form of the ST prediction. Following the work of Warren *et al.* [42], we have estimated the free parameters of the ST model, by maximizing the extended Poisson likelihood. For all cosmologies, the fits have an accuracy of up to 10%-20% at low and intermediate mass bins. We also used only the fit for the fiducial cosmology 2D mass function, to predict the 2D mass functions for the other cosmologies. In this case, the accuracy was of about 20% in the same mass range.

Our goal for the future is to extend our analysis to uncorrelated projections, and to study both theoretical and numerical avenues for the prediction of the shear-peak abundance, and its cosmology dependence. Should such an undertaking be successful, it will establish the WL method for cluster detection as a very reliable way to extract cosmological constraints, limited only by survey systematics.

Acknowledgments

We thank Peter Schneider for carefully reading the manuscript and for his suggestions. LM acknowledges the hospitality of the ITP, University of Zürich, where

some of this project has been developed. RES kindly thanks the Argelander Institute, University of Bonn, for hospitality whilst some of this work was being done. We are grateful to V. Springel for making public GADGET-2 and for providing his B-FoF halo finder; and to R. Scoccamarro for making public his 2LPT code. LM is supported by the Deutsche Forschungsgemeinschaft under the Transregion TRR33 The Dark Universe. RES acknowledges support from a Marie Curie Reintegration Grant and the Swiss National Foundation under contract 200021-116696/1. GMB is supported in this work by grant AST-0607667 from the National Science Foundation, Department of Energy grant DOE-DE-FG02-95ER40893, and NASA grant BEFS-04-0014-0018.

-
- [1] Abate, A., D. Wittman, V. E. Margoniner, S. L. Bridle, P. Gee, J. A. Tyson, and I. P. Dell Antonio, 2009, ArXiv e-prints 0904.2185.
- [2] Albrecht, A., G. Bernstein, R. Cahn, W. L. Freedman, J. Hewitt, W. Hu, J. Huth, M. Kamionkowski, E. W. Kolb, L. Knox, J. C. Mather, S. Staggs, *et al.*, 2006, ArXiv Astrophysics e-prints astro-ph/0609591.
- [3] Bullock, J. S., T. S. Kolatt, Y. Sigad, R. S. Somerville, A. V. Kravtsov, A. A. Klypin, J. R. Primack, and A. Dekel, 2001, Mon. Not. R. Astron. Soc. **321**, 559.
- [4] Clowe, D., G. De Lucia, and L. King, 2004, Mon. Not. R. Astron. Soc. **350**, 1038.
- [5] Cooray, A., and R. Sheth, 2002, Phys. Rep. **372**, 1.
- [6] Crocce, M., P. Fosalba, F. J. Castander, and E. Gaztanaga, 2009, ArXiv e-prints 0907.0019.
- [7] Davis, M., G. Efstathiou, C. S. Frenk, and S. D. M. White, 1985, Astrophys. J. **292**, 371.
- [8] De Putter, R., and M. White, 2005, New Astronomy **10**, 676.
- [9] Dietrich, J. P., and J. Hartlap, 2009, ArXiv e-prints 0906.3512.
- [10] Dodelson, S., 2004, Phys. Rev. D **70**(2), 023008.
- [11] Hamana, T., M. Takada, and N. Yoshida, 2004, Mon. Not. R. Astron. Soc. **350**, 893.
- [12] Hennawi, J. F., and D. N. Spergel, 2005, Astrophys. J. **624**, 59.
- [13] Hoekstra, H., 2001, Astron. Astrophys. **370**, 743.
- [14] Hoekstra, H., Y. Mellier, L. van Waerbeke, E. Semboloni, L. Fu, M. J. Hudson, L. C. Parker, I. Tereno, and K. Benabed, 2006, Astrophys. J. **647**, 116.
- [15] Hu, W., and A. V. Kravtsov, 2003, Astrophys. J. **584**, 702.
- [16] Jarvis, M., G. M. Bernstein, P. Fischer, D. Smith, B. Jain, J. A. Tyson, and D. Wittman, 2003, Astron. J. **125**, 1014.
- [17] Jarvis, M., B. Jain, G. Bernstein, and D. Dolney, 2006, Astrophys. J. **644**, 71.
- [18] Komatsu, E., J. Dunkley, M. R. Nolta, C. L. Bennett, B. Gold, G. Hinshaw, N. Jarosik, D. Larson, M. Limon, L. Page, D. N. Spergel, M. Halpern, *et al.*, 2009, Astrophys. J. Supp. **180**, 330.
- [19] Kratochvil, J. M., Z. Haiman, and M. May, 2009, ArXiv e-prints 0907.0486.
- [20] Kruse, G., and P. Schneider, 1999, Mon. Not. R. Astron. Soc. **302**, 821.
- [21] Marian, L., and G. M. Bernstein, 2006, Phys. Rev. D **73**(12), 123525.
- [22] Marian, L., R. E. Smith, and G. M. Bernstein, 2009, Astrophys. J. Lett. **698**, L33.
- [23] Maturi, M., M. Meneghetti, M. Bartelmann, K. Dolag, and L. Moscardini, 2005, Astron. Astrophys. **442**, 851.
- [24] Maturi, M., M. Schirmer, M. Meneghetti, M. Bartelmann, and L. Moscardini, 2007, Astron. Astrophys. **462**, 473.
- [25] Metzler, C. A., M. White, and C. Loken, 2001, Astrophys. J. **547**, 560.
- [26] Moore, B., S. Ghigna, F. Governato, G. Lake, T. Quinn, J. Stadel, and P. Tozzi, 1999, Astrophys. J. Lett. **524**, L19.
- [27] Navarro, J. F., C. S. Frenk, and S. D. M. White, 1997, Astrophys. J. **490**, 493.
- [28] Pires, S., J. Starck, A. Amara, A. Refregier, and R. Teyssier, 2009, ArXiv e-prints 0904.2995.
- [29] Reblinsky, K., G. Kruse, B. Jain, and P. Schneider, 1999, Astron. Astrophys. **351**, 815.
- [30] Schirmer, M., T. Erben, M. Hettterscheidt, and P. Schneider, 2007, Astron. Astrophys. **462**, 875.
- [31] Schneider, P., 1996, Mon. Not. R. Astron. Soc. **283**, 837.
- [32] Schneider, P., L. van Waerbeke, B. Jain, and G. Kruse, 1998, Mon. Not. R. Astron. Soc. **296**, 873.
- [33] Scoccamarro, R., 1998, Mon. Not. R. Astron. Soc. **299**, 1097.
- [34] Seljak, U., and M. Zaldarriaga, 1996, Astrophys. J. **469**, 437.
- [35] Semboloni, E., Y. Mellier, L. van Waerbeke, H. Hoekstra, I. Tereno, K. Benabed, S. D. J. Gwyn, L. Fu, M. J. Hudson, R. Maoli, and L. C. Parker, 2006, Astron. Astrophys. **452**, 51.
- [36] Sheth, R. K., and G. Tormen, 1999, Mon. Not. R. Astron. Soc. **308**, 119.
- [37] Smith, R. E., and P. I. R. Watts, 2005, Mon. Not. R. Astron. Soc. **360**, 203.
- [38] Spergel, D. N., L. Verde, H. V. Peiris, E. Komatsu, M. R. Nolta, C. L. Bennett, M. Halpern, G. Hinshaw, N. Jarosik, A. Kogut, M. Limon, S. S. Meyer, *et al.*, 2003, Astrophys. J. Supp. **148**, 175.

- [39] Springel, V., 2005, *Mon. Not. R. Astron. Soc.* **364**, 1105.
- [40] Tang, J. Y., and Z. H. Fan, 2005, *Astrophys. J.* **635**, 60.
- [41] Wang, S., J. Khoury, Z. Haiman, and M. May, 2004, *Phys. Rev. D* **70**(12), 123008.
- [42] Warren, M. S., K. Abazajian, D. E. Holz, and L. Teodoro, 2006, *Astrophys. J.* **646**, 881.